

## Electronic Supplementary Information (ESI)

# Ni-decorated carbon nanotubes (CNTs) derived from ethanol for electrooxidation of furan derivatives featuring H<sub>2</sub> production

*Watinee Nunthakitgoson, Peeranat Chaipornchalerms, Anousha Sohail, Anawat Thivasasith, and Chularat Wattanakit\**

*Department of Chemical and Biomolecular Engineering, School of Energy Science and Engineering, Vidyasirimedhi Institute of Science and Technology, Rayong, 21210, Thailand*

\*Email: [chularat.w@vistec.ac.th](mailto:chularat.w@vistec.ac.th)

## Experimental Section

### Materials

All chemicals utilized in this study were of analytical grade and used as obtained without any further purification. For zeolite synthesis, tetraethyl orthosilicate (TEOS, Sigma-Aldrich), sodium aluminate ( $\text{NaAlO}_2$ , Sigma-Aldrich), aluminum isopropoxide ( $\text{C}_9\text{H}_{21}\text{O}_3\text{Al}$ , Sigma-Aldrich), and sodium fluoride ( $\text{NaF}$ , Carlo Erba) were used as silica precursor, alumina precursor, and mineralizing agent, respectively. Tetra (n-butyl) ammonium hydroxide (TBAOH, Leonid Chemicals) was used as the structure-directing agent (SDA). After obtaining the synthesized zeolites, nickel (II) nitrate hexahydrate ( $\text{Ni}(\text{NO}_3)_2 \cdot 6\text{H}_2\text{O}$ , Merck) was used as the transition metal precursors for the preparation of the metal-based catalyst for CNTs production. Ammonium chloride ( $\text{NH}_4\text{Cl}$ , Kemaus) was used to prepare the acid zeolite. Bioethanol, obtained through sugar fermentation and supplied by KTIS Company in Rayong, Thailand, is used as a carbon precursor for CNTs production. 5-hydroxymethylfurfural (5-HMF, Tokyo Chemical Industry) and Furfural (FF, Sigma-Aldrich) were employed as the starting substances for electrocatalysis. 2,5-furan dicarboxylic acid (FDCA, Tokyo Chemical Industry Co. Ltd), 5-formyl-2-furan carboxylic acid (FFCA, Tokyo Chemical Industry Co. Ltd), 2,5-diformylfuran (DFF, Tokyo Chemical Industry Co. Ltd), and 5-hydroxymethyl-2-furan carboxylic acid (HMFCA, Tokyo Chemical Industry Co. Ltd) were used for the qualitative and quantitative analysis in the reaction study. Milli-Q water ( $18.2 \text{ M}\Omega \text{ cm}$ ), potassium hydroxide ( $\text{KOH}$ , Sigma-Aldrich), and nickel foam (NF, Celmet #8, Sumitomo Electric Industries Ltd., Japan) were used for electrocatalytic testing. Methanol ( $\text{CH}_3\text{OH}$ , RCI Labscan), acetonitrile ( $\text{C}_2\text{H}_3\text{N}$ , RCI labscan), and sulfuric acid ( $\text{H}_2\text{SO}_4$ , QR  c) were used as a mobile phase for HPLC analysis.

### Synthesis of powder hierarchical ZSM-5 (HieZSM-5)

Hierarchical ZSM-5 zeolite was synthesized using a hydrothermal method following the adapted literature procedure. At first, the precursor was prepared with the molar composition of  $60 \text{ SiO}_2$ :  $0.6 \text{ Al}_2\text{O}_3$ :  $18 \text{ TBAOH}$ :  $0.75 \text{ NaF}$ :  $600 \text{ H}_2\text{O}$ :  $240 \text{ EtOH}$ .<sup>1</sup> In brief, TEOS, TBAOH, and  $\text{C}_9\text{H}_{21}\text{AlO}_3$  were dissolved in an alkaline solution to produce a sodium aluminate solution, which was agitated continuously overnight at room temperature before transferring to a hydrothermal autoclave reactor for the crystallization process. The temperature of the reactor was subsequently heated to  $130^\circ\text{C}$  for 2 days. The obtained solid product was collected, washed with DI water to neutralize the pH of the filtrate, and dried overnight at  $100^\circ\text{C}$ . The synthesized white powder was then calcined at  $550^\circ\text{C}$  for 6 h to remove the structure-directing agent (SDA). The final product was designated as HieZSM-5.

### Preparation of the hierarchical ZSM-5 as the ethanol dehydration catalyst (HieHZSM-5)

Indeed, the obtained  $\text{Na}^+$  formed HieZSM-5 catalyst from the above-mentioned procedure was converted to the acid form by ion exchange with a  $0.1 \text{ M NH}_4\text{Cl}$  solution at  $80^\circ\text{C}$  for 2 h, repeated in three cycles. Subsequently, the prepared zeolites were dried and calcined at  $550^\circ\text{C}$  for 4 h to convert into acid form. Finally, the acid ZSM-5 (HieHZSM-5) was obtained. Before applying as a catalyst in bioethanol dehydration, the catalyst was sieved to a particle size in the range of 428 to  $850 \mu\text{m}$ .

### Synthesis of conventional ZSM-5 (CONZSM-5)

A conventional ZSM-5 zeolite (CONZSM-5) was synthesized using a hydrothermal method based on a previously described procedure.<sup>2</sup> Briefly, tetraethyl orthosilicate (TEOS), tetrapropylammonium hydroxide (TPAOH), and deionized (DI) water were mixed to form solution A. Separately, sodium aluminate ( $\text{NaAlO}_2$ ), DI water, and sodium hydroxide (NaOH) were combined to form solution B. Solution A was then added to solution B and mixed at ambient temperature and pressure for 2 h. The resulting gel was transferred to a 100 mL autoclave and subjected to crystallization at 180°C for 3 days. The obtained white powder was dried and calcined at 550°C for 6 h to remove the SDA. The final product was designated as CONZSM-5.

### **Preparation of nickel (Ni) supported on hierarchical and conventional ZSM-5 zeolites by a conventional wet impregnation method**

The nickel nanoparticles supported on as-synthesized hierarchical ZSM-5 zeolites (HieZSM-5) were prepared by the wet impregnation method. Initially, nickel (II) nitrate hexahydrate ( $\text{Ni}(\text{NO}_3)_2 \cdot 6\text{H}_2\text{O}$ ) (0.124 g) was dissolved in 10 mL of DI water. Subsequently, 0.5 g of hierarchical ZSM-5 zeolite was added to the prepared metal solution under vigorous stirring at room temperature for 2 h. The solvent was then evaporated using a rotary vacuum evaporator, and the acquired powder was dried overnight at 100 °C for 24 h. Afterward, the obtained nickel-supported zeolites were calcined at 550 °C for 4 h. For the incorporation of nickel on conventional ZSM-5 zeolite (CONZSM-5), a similar preparation procedure to the above-described procedure was applied. The prepared sample was denoted as 5wt.%NixZSM-5, where x refers to CON and Hie for conventional and hierarchical ZSM-5, respectively.

### **Synthesis of carbon nanotube (CNTs) on nickel oxide supported on ZSM-5 using bioethanol as carbon source**

For the CNTs production, the two-step process performed on a dual fixed-bed reactor was applied as shown in Scheme S2.<sup>3</sup> In the first reactor, catalytic bioethanol dehydration to ethylene was obtained using the HieHZSM-5 as an acid catalyst. At first, the HieHZSM-5 (0.1 g) was added to the middle position of the stainless-steel tube, which was placed in a fixed-bed reactor. Subsequently, the catalyst was pretreated with  $\text{N}_2$  (40 mL min<sup>-1</sup>) at 350°C for 1 h. In the second reactor, the CNTs synthesis via the CVD process from the produced bioethylene as a carbon source obtained from the first reactor was taken place. Prior to the CNTs synthesis, the 0.1 g of 5wt%NixZSM-5 as a catalyst was pretreated with the 5 % v/v of  $\text{H}_2$  in Ar (40 mL min<sup>-1</sup>) for 1 h at 550 °C at the second reactor. After the pretreatment process, the temperature of the first and second reactors was optimized to 350 °C and 700 °C, respectively, in the continuous  $\text{N}_2$  gas flow. Subsequently, 0.5 g.h<sup>-1</sup> of bioethanol with the  $\text{N}_2$  flow rate of 9 mL min<sup>-1</sup> was introduced into the first reactor to produce bioethylene. After that, bioethylene was fed into the second reactor for CNTs production via the CVD process for 1 h. The final products are denoted as NixZSM-5-CNTs, where x relates to CON and Hie, corresponding to conventional and hierarchical ZSM-5 zeolites, respectively.

### **Characterization**

The diffraction patterns and crystallinity of the synthesized zeolites were analyzed using X-ray diffraction (XRD) with a Bruker D8 advanced powder diffractometer. Measurements were taken with a step size of 0.08° and a scan rate of 1° min<sup>-1</sup> over a 2θ range of 5 to 60°. The elemental composition of the prepared catalysts was determined by X-ray fluorescence spectrometry (XRF) using a Bruker S8 Tiger ECO model. The morphology of the catalysts and CNTs was examined using scanning electron microscopy (SEM) on a JEOL JSM-7610F (2 kV) and transmission electron microscopy (TEM) on a JEOL JEM-200F (200

kV). X-ray photoelectron spectroscopy (XPS) was performed using a JEOL JPS-9010 with Twin anode (Mg K $\alpha$  source at 1253.6 eV and Al K $\alpha$  source at 1486.6 eV) at 12 kV and 25 mA. Prior to measurement, the samples were pretreated with Ar to clean the surface for 5 seconds under a high vacuum of  $10^{-8}$  Pa at room temperature. Textural properties of the catalysts were determined through N $_2$  adsorption/desorption measurements at -196 °C using a MicrotracBEL, BELSORP-max model, with samples degassing at 300 °C for 24 h before measurement. Specific surface area ( $S_{\text{BET}}$ ), micropore surface area ( $S_{\text{micro}}$ ), and pore volume ( $V_{\text{total}}$ ) were calculated using the Brunauer–Emmett–Teller (BET) and  $t$ -plot methods.

The CNTs content was evaluated via thermogravimetric analysis and differential thermal analysis (TGA-DTA) on an STA PT 1600/Linseis instrument. Samples were heated from ambient temperature to 900 °C at a rate of 10 °C min $^{-1}$  under an oxygen flow (100 mL min $^{-1}$ ). The structures of the CNTs were further characterized using Dispersive Raman Spectroscopy on a Bruker SENTERRA spectrometer, utilizing a 532 nm Nd-YAG laser with a 5 mW output, focusing the beam with a 20x objective, and collecting results in the 50 to 2700 cm $^{-1}$  range. The  $I_D/I_G$  ratio was also described using Raman spectroscopy.

Inductively coupled plasma-optical emission spectroscopy (ICP-OES) was used to quantify the metal content of the samples, utilizing an Agilent Technologies 700 series instrument. Prior to analysis, the samples were digested with a mixture of concentrated hydrofluoric acid (HF), hydrochloric acid (HCl), and nitric acid (HNO $_3$ ) in a volume ratio of 2:3:3.

## Electrochemical testing

### Fabrication of NiCNTs supported on nickel foam as a working electrode

To fabricate the working electrodes, 4 mL of 48% hydrofluoric acid (HF) was added to 0.1 g of the NiZSM-5-CNTs composite to extract the zeolite from the Ni-supported CNTs composite. The resulting mixture was stirred for 12 h at room temperature. Subsequently, the Ni nanoparticles supported on CNTs were isolated by washing the residue with deionized water, and the obtained powder was then dried at 100 °C for 12 h. The dried powder was designated as NiCNTs. The working electrodes were prepared by dispersing 0.1 mg of the NiCNTs powder into isopropanol, followed by dropping it onto compressed nickel foam with an area of 1.0 cm $^2$ .

## Electrochemical Experiment

### Three-electrode setup for electrochemical measurement

Electrochemical measurements were conducted using an Autolab/PGSTAT 204 potentiostat. Cyclic voltammetry (CV) and linear sweep voltammetry (LSV) were performed in the H-type cell with a three-electrode setup, employing NiCNTs/NF as the working electrode, a platinum mesh as the counter electrode, and an Hg/HgO as the reference electrode.

We conducted Linear Sweep Voltammetry (LSV) measurements over a potential range of 0 to 0.7 V vs. Hg/HgO at a scan rate of 20 mV s $^{-1}$  in a 1.0 M KOH solution. For the electrooxidation of 5-hydroxymethylfurfural (5-HMF) and furfural, the LSV experiments were performed with varying concentrations of 5-HMF (2 to 10 mM) or 5 mM furfural. Additionally, for the hydrogen evolution reaction (HER), LSV measurements were conducted within the potential range of 0.6 to -1.3 V vs. Hg/HgO at the same scan rate of 20 mV s $^{-1}$ . All reported potentials in this study were converted to the reversible hydrogen electrode (RHE) scale using the given equation (1):

$$E_{\text{RHE}} = E_{\text{Hg/HgO}} + 0.059(\text{pH}) + 0.098 \text{ V} \quad (1)$$

Using the LSV data, we constructed Tafel plots to analyze the kinetic behavior of the electrochemical reaction. By plotting the overpotential ( $\eta$ ) against the logarithm of the current density

(log J), we were able to fit the linear portion of the curve with the Tafel equation. This fitting process enabled us to determine the Tafel slope (b) and the intercept (a), which are critical parameters in understanding the reaction kinetics. The linear portion of the plot is fitted to the Tafel equation as shown below:

$$\eta = a + b \log(J) \quad (2)$$

Where b is the Tafel slope, and a is the intercept.

We also performed Electrochemical Impedance Spectroscopy (EIS) measurements. These were conducted in a 1 M KOH solution over a frequency range from 0.01 Hz to 100 kHz, using an AC amplitude of 10 mV. To gain insights into the reaction mechanisms, we fitted the EIS data to an equivalent circuit model, which allowed us to extract key parameters, including the charge transfer resistance ( $R_{ct}$ ).

The electrochemically active surface area (ECSA) was calculated by equation (3), where the double-layer capacitance ( $C_{dl}$ ) was calculated from CV curves recorded in a potential range with no faradaic current at different scan rates ranging from 10 to 60 mV s<sup>-1</sup> vs.Hg/HgO. The ECSA of the catalysts was calculated according to the equation (3):

$$ECSA = C_{dl}/C_s \quad (3)$$

Where  $C_s$  can be defined as the specific capacitance of the material per unit area under identical electrolyte conditions (0.040 mF.cm<sup>-2</sup>)<sup>4</sup>.

### **Two-electrode setup for the combined cell of concurrent 5-HMF or furfural electrooxidation and hydrogen production**

After obtaining the optimal potentials required for individual 5-HMF/furfural electrooxidation and hydrogen electroreduction at anode and cathode, respectively, those potentials were used to calculate the cell voltage as shown in Eq. (4):

$$E_{cell} = |E_{cathode \text{ vs RHE}} - E_{anode \text{ vs RHE}}| \quad (4)$$

where  $E_{cathode \text{ vs RHE}}$  and  $E_{anode \text{ vs RHE}}$ : Cathode or anode potential vs. RHE.

Two-electrode setup (NiCNTs/NF) was employed for investigating stability, kinetic studies, and catalytic performance of the NiCNTs/NF electrodes, which can be used for both cathode and anode as shown in Scheme S3. The electrooxidation part was studied in 1M KOH with 5 mM 5-HMF, where liquid products were analyzed using HPLC. For the quantitative investigation of the gaseous product from HER, the collected gas was analyzed by gas chromatography with a thermal conductivity detector (TCD) using the Select Permanent Gases/CO<sub>2</sub> with continuous nitrogen flow through the H-type anodic compartment.

### **Quantitative product analysis**

The products were analyzed by employing High-Performance Liquid Chromatography (HPLC, Shimadzu Prominence (LC-40D) model) system equipped with a Photodiode Array (PDA) detector (SPD-M40). A mobile phase containing 85% of 10 mM H<sub>2</sub>SO<sub>4</sub> (sulfuric acid), 10% methanol, and 5% acetonitrile (v/v) was applied at a flow rate of 0.3 mL min<sup>-1</sup> at 30 °C. Sample aliquots of 5 µL were injected into a C18 column (Inertsil ODS-3, 3 µm, 4.6 × 250 mm) for separation. Calibration curves for both reactant and products, including 5-HMF, HMFCA, FFCA, and FDCA, were established at a detection wavelength at 238 nm. The calibration curve for DFF was determined at 288 nm and the wavelength of 245 and 276 nm for

2-FA and FF, respectively (see Fig S16). The amount of hydrogen produced, and its Faradaic efficiency were measured by gas chromatography (GC). Aliquots were collected every 20 minutes for HPLC analysis to quantify organic chemicals and determine their Faradaic efficiency.

To determine the conversion and yield of the organic substrate, the following formulae were used:

$$\text{Conversion of reactant (HMF or FF) (\%)} = \frac{\text{moles of consumed reactant}}{\text{moles of initial reactant}} \times 100 \quad (5)$$

$$\text{Yield of the product (FDCA or 2-FA) (\%)} = \frac{\text{moles of desired product}}{\text{moles of initial reactant}} \times 100 \quad (6)$$

$$\text{Selectivity of the product (FDCA or 2-FA) (\%)} = \frac{\text{moles of desired product}}{\text{moles of consumed reactant}} \times 100 \quad (7)$$

The faradaic efficiency (FE) of product formation in the anodic part was calculated using the equation (8):

$$\text{Faradaic efficiency (FE) (\%)} = \frac{n \times F \times \text{moles of formed product}}{Q} \times 100 \quad (9)$$

Where n is the number of electrons transferred for each product molecule; F is the Faraday constant (96,485 C mol<sup>-1</sup>); and Q is the transferred charge.

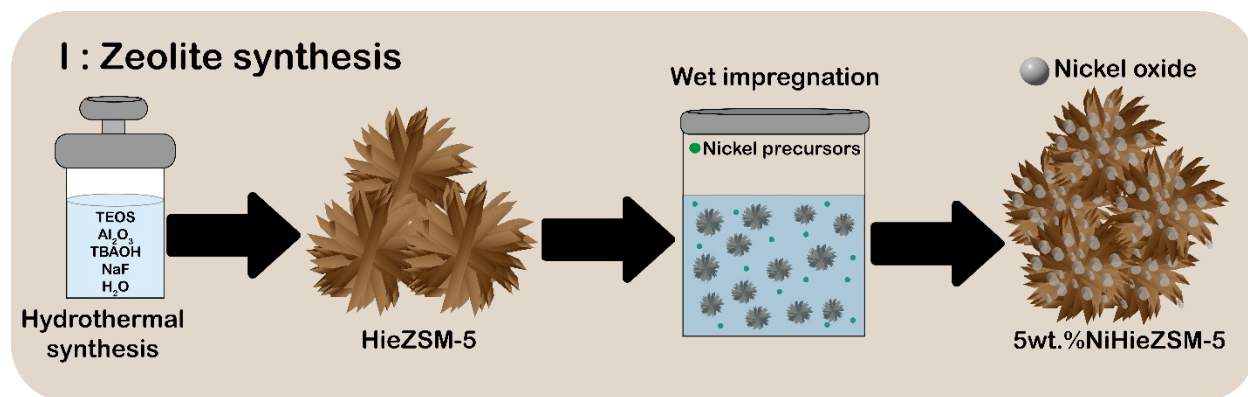
The faradaic efficiency (FE) of hydrogen formation in the cathodic part was calculated using the equation (10):

$$\text{Faradaic efficiency (FE) (\%)} = \frac{\text{moles of hydrogen production}}{\text{moles of theoretical hydrogen production}} \times 100 \quad (10)$$

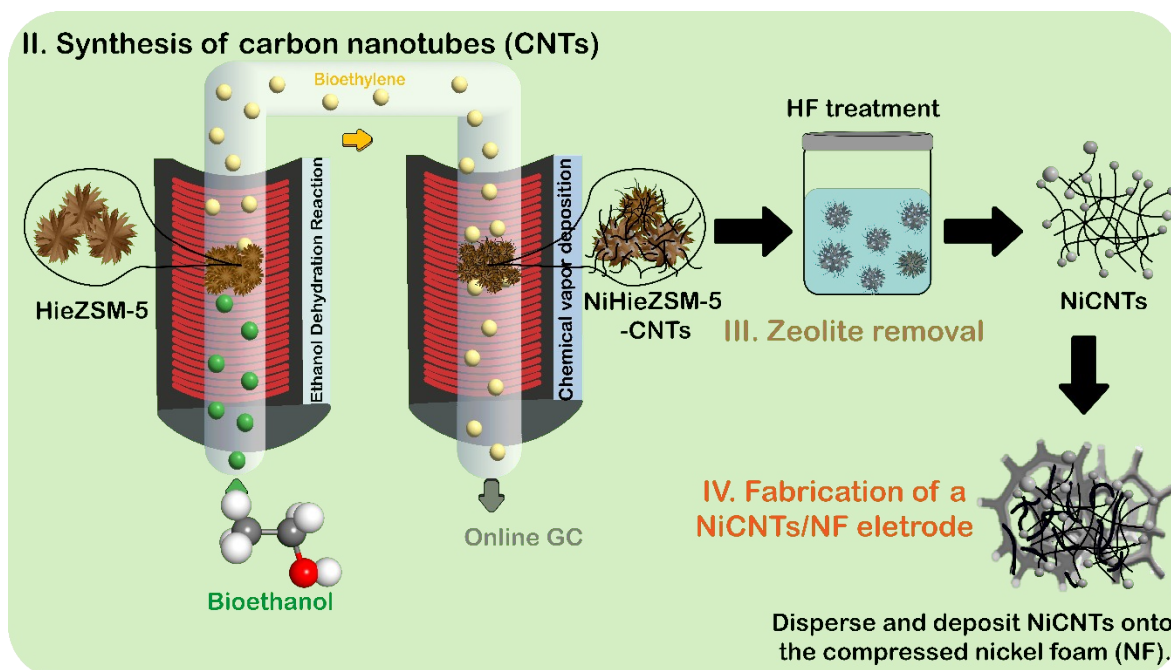
The quantity based on theoretical production was determined using the following equation:

$$\text{Moles of theoretically produced hydrogen} = \frac{Q}{n \times F} \quad (11)$$

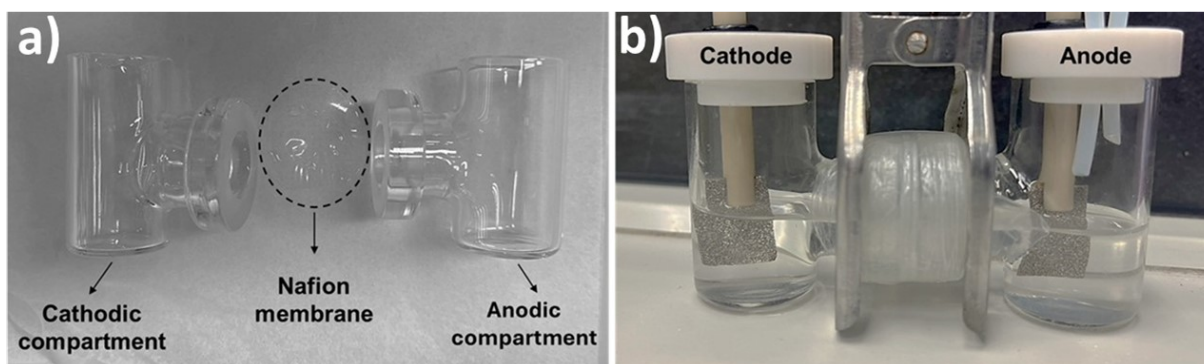
Q is the transferred charge; n is the number of electrons transferred for each product molecule; and F is the Faraday constant (96,485 C mol<sup>-1</sup>).



**Scheme S1 (I)** Schematic illustration of ZSM-5 zeolite synthesis via hydrothermal approach and preparation of nickel (Ni) supported on ZSM-5 zeolite using the wet impregnation method.



**Scheme. S2** Synthesis of carbon nanotubes (CNTs) and fabrication of the NiCNTs deposited on nickel foam (NiCNTs/NF) for simultaneous biorefinery oxidation and  $H_2$  production.



**Scheme. S3** (a) Experimental setup and (b) setup of the H-cell used for all electrochemical experiments, with a Nafion-115 membrane used to separate the anodic and cathodic compartments.

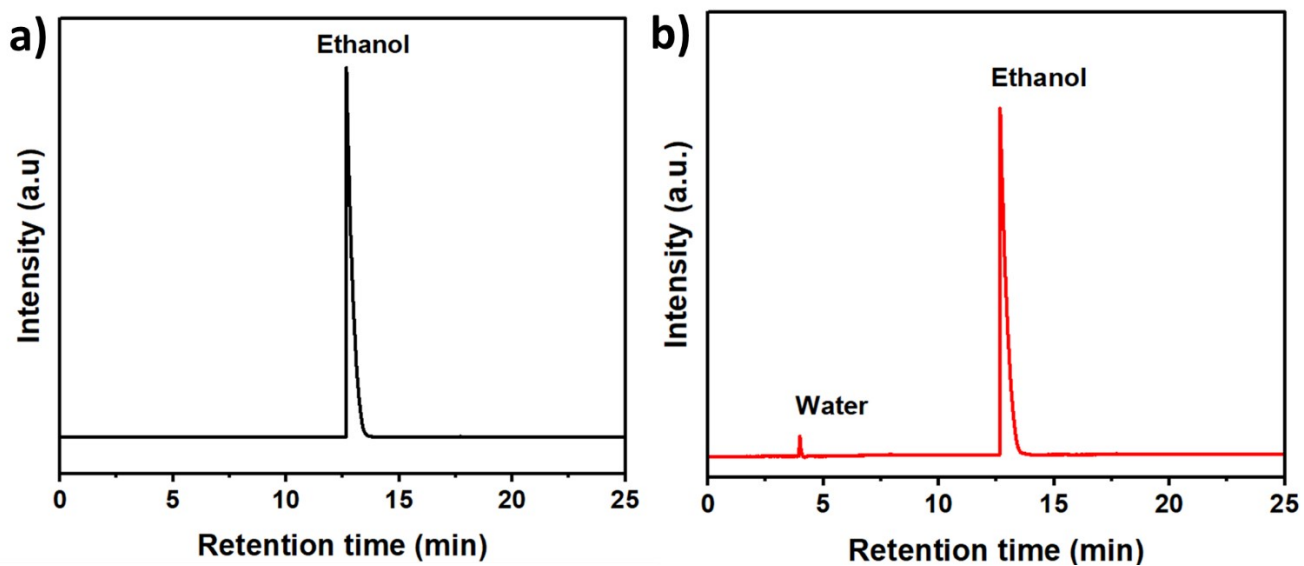


**Fig. S1** (a) GC-FID and (b) GC-TCD chromatograms of bioethanol obtained through the fermentation of sugar by the KTIS company in Rayong, Thailand.

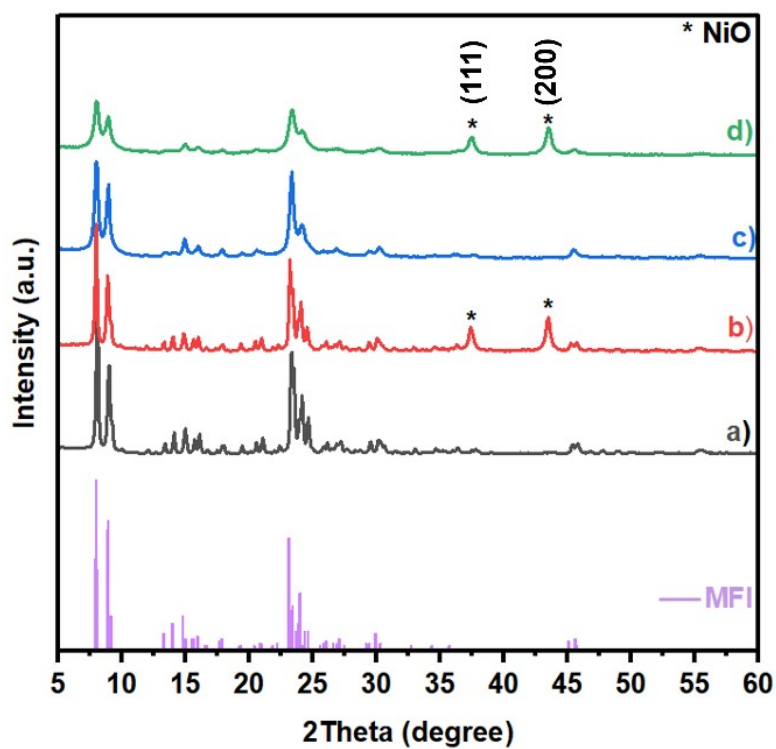


**Fig. S2** XRD patterns (a) pristine CONZSM-5, (b) 5wt.%NiCONZSM-5, (c) pristine HieZSM-5, and (d) 5wt.%NiHieZSM-5.



**Table S1** The chemical compositions of synthesized catalysts and Ni supported on ZSM-5 obtained by XRF measurements.

Sample	Composition (% wt.)			
	SiO <sub>2</sub>	Al <sub>2</sub> O <sub>3</sub>	Ni	Si/Al
CONZSM-5	92.9	0.9	-	75.3
5wt.%NiCONZSM-5	86.4	1.1	5.1	66.7
HieZSM-5	98.5	1.1	-	73.3
5wt%.NiHieZSM-5	85.4	1.2	5.1	69.8

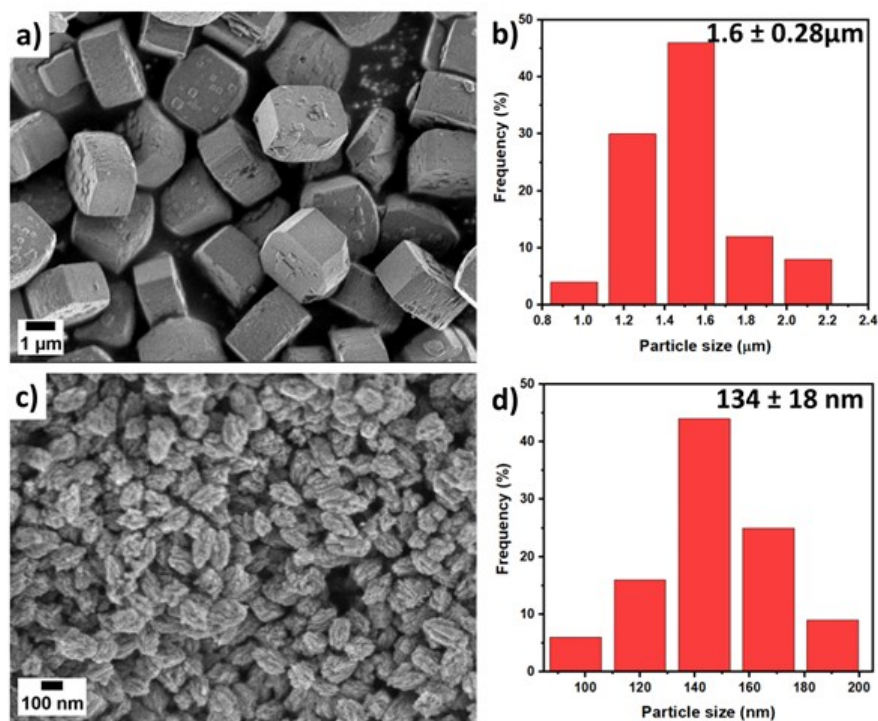


**Fig. S3** SEM images and their corresponding particle size distribution of (a,b) 5 wt.% NiCONZSM-5 and (c,d) 5 wt.% NiHieZSM-5 zeolite.

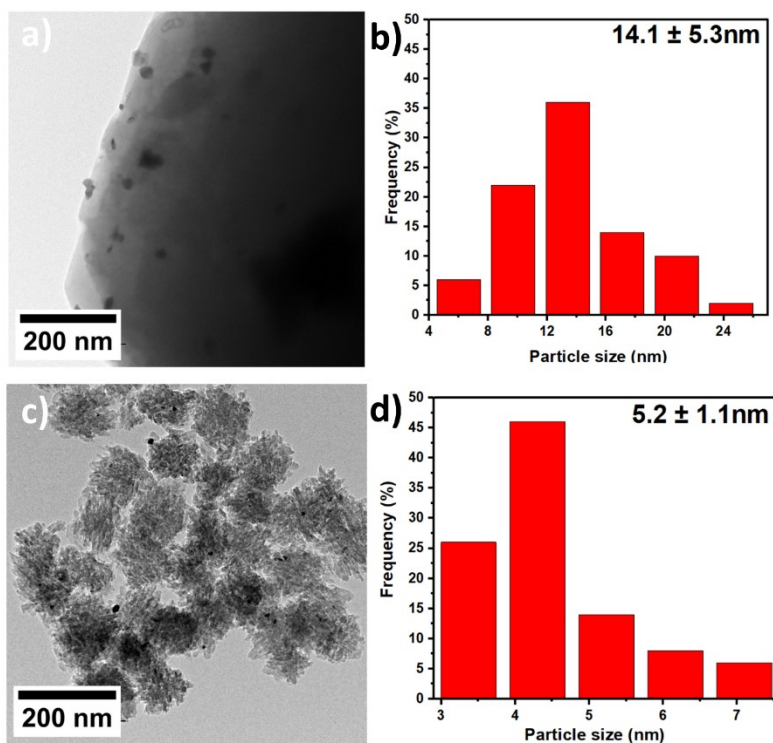


**Fig. S4** TEM image and average particle size distribution of Ni metal supported on (a,b) 5 wt.% NiCONZSM-5 and (c,d) 5 wt.% NiHieZSM-5.

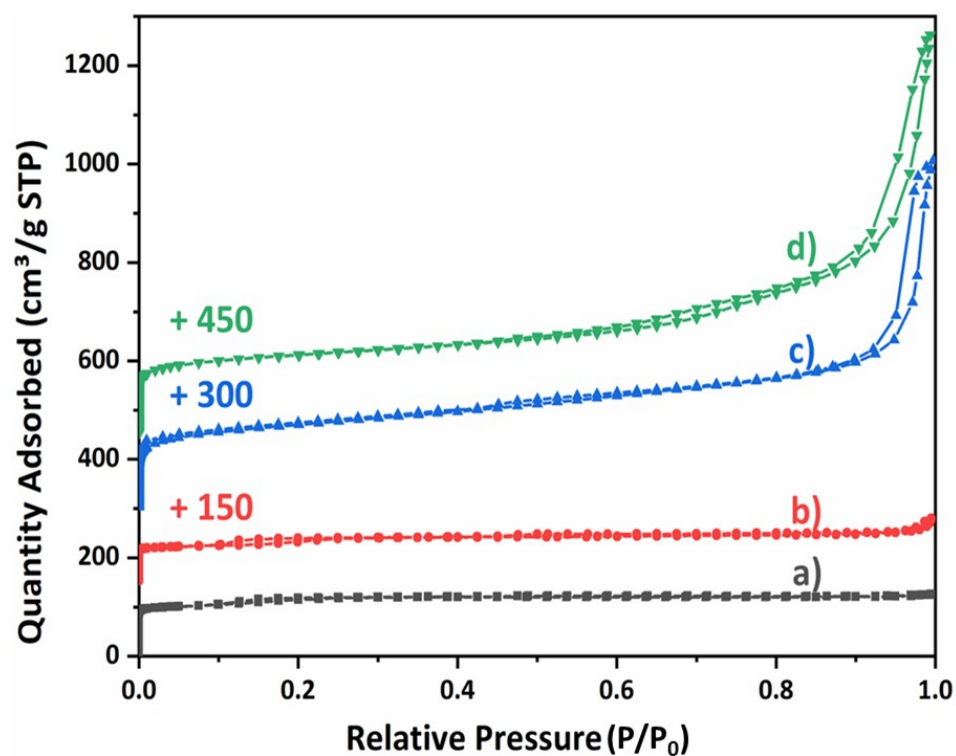


**Fig. S5** N<sub>2</sub> physisorption isotherms of (a) pristine CONZSM-5, (b) 5wt.%NiCONZSM-5, (c) pristine HieZSM-5, and (d) 5wt.% NiHieZSM-5.

**Table S2** Textural properties of conventional and hierarchical ZSM-5 and Ni supported on conventional and hierarchical ZSM-5.

Sample	$S_{\text{BET}}^{\text{a}}$ (m <sup>2</sup> /g)	$S_{\text{micro}}^{\text{b}}$ (m <sup>2</sup> /g)	$S_{\text{ext}}^{\text{b}}$ (m <sup>2</sup> /g)	$V_{\text{total}}^{\text{c}}$ (cm <sup>3</sup> /g)	$V_{\text{micro}}^{\text{b}}$ (cm <sup>3</sup> /g)	$V_{\text{ext}}^{\text{b}}$ (cm <sup>3</sup> /g)
CONZSM-5	553.0	401.9	151.1	0.24	0.17	0.07
5wt.% NiCONZSM-5	398.3	252.5	145.7	0.18	0.10	0.08
HieZSM-5	610.8	305.0	305.8	0.53	0.13	0.40
5wt.% NiHieZSM-5	429.4	233.4	196.0	0.41	0.10	0.31

<sup>a</sup>  $S_{\text{BET}}$ : Surface area calculated using the BET method

<sup>b</sup>  $S_{\text{micro}}$ ,  $S_{\text{ext}}$ ,  $V_{\text{micro}}$ , and  $V_{\text{ext}}$ : Micropore surface area, external surface area, micropore volume calculated using a *t*-plot method, and external pore volume ( $V_{\text{ext}} = V_{\text{total}} - V_{\text{micro}}$ )

<sup>c</sup>  $V_{\text{total}}$ : Total pore volume at a relative pressure of 0.99

The textural properties of the as-synthesized catalyst were determined by N<sub>2</sub> sorption isotherms, as presented in Fig. S5 and Table S2. It should be noted that both CONZSM-5 and 5 wt% NiCONZSM-5 follow the type I isotherm, indicating the presence of microporous structures. Conversely, HieZSM-5 and 5 wt% NiHieZSM-5 exhibited the combined types I and IV, confirming hierarchical structures containing micropores and mesopores. Indeed, nickel incorporation on zeolites led to reduced surface area and porosity due to the pore blockage from nickel nanoparticles.

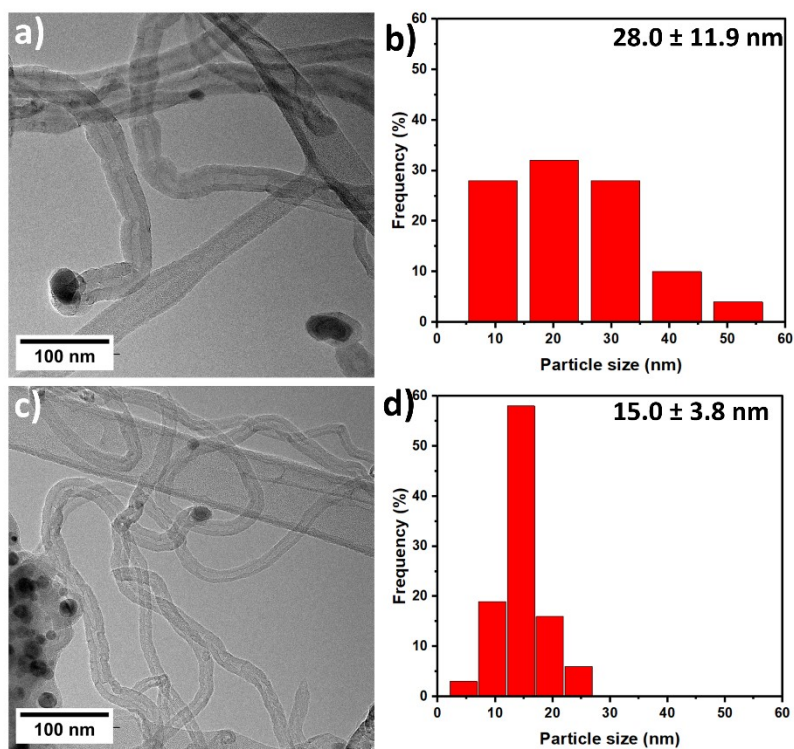


**Fig. S6** TEM image and average metal particle size distribution on (a,b) NiCONZSM-5-CNTs, and (c,d) NiHieZSM-5-CNTs after CNTs growth process.

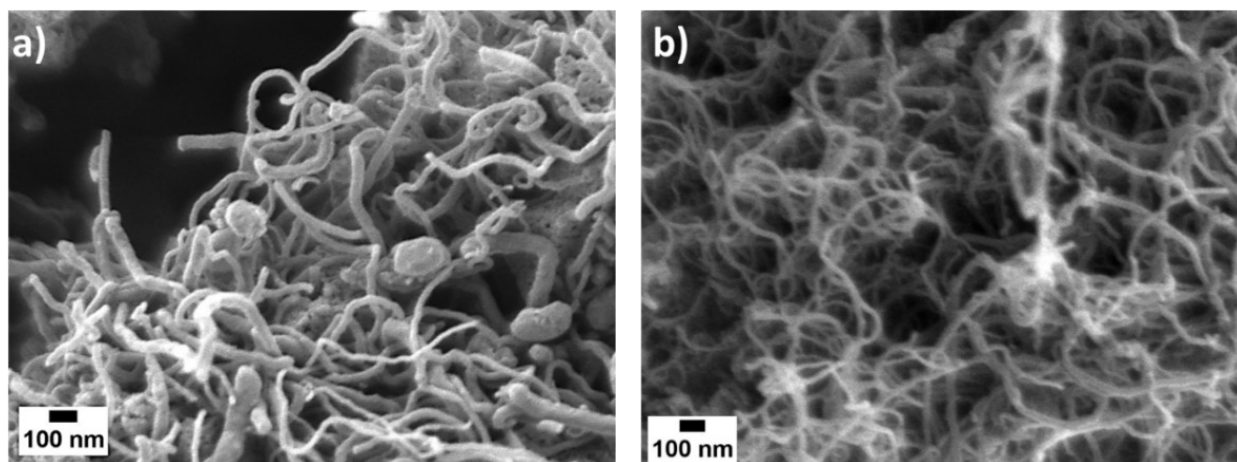


**Fig. S7** SEM image of (a) NiCONZSM-5-CNTs, and (b) NiHieZSM-5-CNTs.

CNTs formed on 5 wt.% NiCONZSM-5 exhibited inner diameters of  $14.2 \pm 3.4$  nm and outer diameters of  $26.2 \pm 2.51$  nm. In contrast, smaller CNTs with inner diameters of  $9.4 \pm 3.4$  nm and outer diameters of  $13.0 \pm 5.2$  nm were formed using 5 wt% NiHieZSM-5 (Table S3, ESI<sup>†</sup>). The large CNT diameters observed with the 5 wt% NiCONZSM-5 catalyst can be attributed to nickel aggregation due to metal sintering during the CNT growth process at high temperatures. In strong contrast, the good dispersion of Ni active sites on HieZSM-5 leads to the formation of smaller carbon nanotubes (CNTs)

**Table S3** The characteristics of CNTs grown over the various catalysts at 700 °C for 1 h and the WHSV of 5 h<sup>-1</sup>.

Sample	CNTs yield (%) <sup>a</sup>	Outer Diameter (nm) <sup>b</sup>	Inner Diameter (nm) <sup>b</sup>	Number of walls <sup>b</sup>	$I_D/I_G$ <sup>c</sup>
NiCONZSM-5-CNTs	10.4	26.2 ± 2.51	14.2±3.4	25-37	1.12
NiHieZSM-5-CNTs	21.8	13.0±5.2	9.4±3.4	10-22	0.62

<sup>a</sup> CNTs yield analyzed by thermogravimetric analysis (TGA), <sup>b</sup> Outer Diameter (nm), inner Diameter (nm) number of walls observed through Transmission Electron Microscopy (TEM), <sup>c</sup>  $I_D/I_G$  analyzed through FT-Raman spectroscopy.

The relative intensity ratio ( $I_D/I_G$ ) of the D and G bands (1336 and 1589  $\text{cm}^{-1}$ , respectively) was used to assess the quality of the CNTs. A lower ID/IG ratio, indicating higher graphitic behavior, was observed with the NiHieZSM-5 catalyst. TGA analysis showed CNT yields of approximately 10.4% for NiCONZSM-5 and 21.8% for NiHieZSM-5, based on % weight loss between 350 and 650 °C. These findings confirm the superior yield and quality of CNTs obtained with the NiHieZSM-5 catalyst.

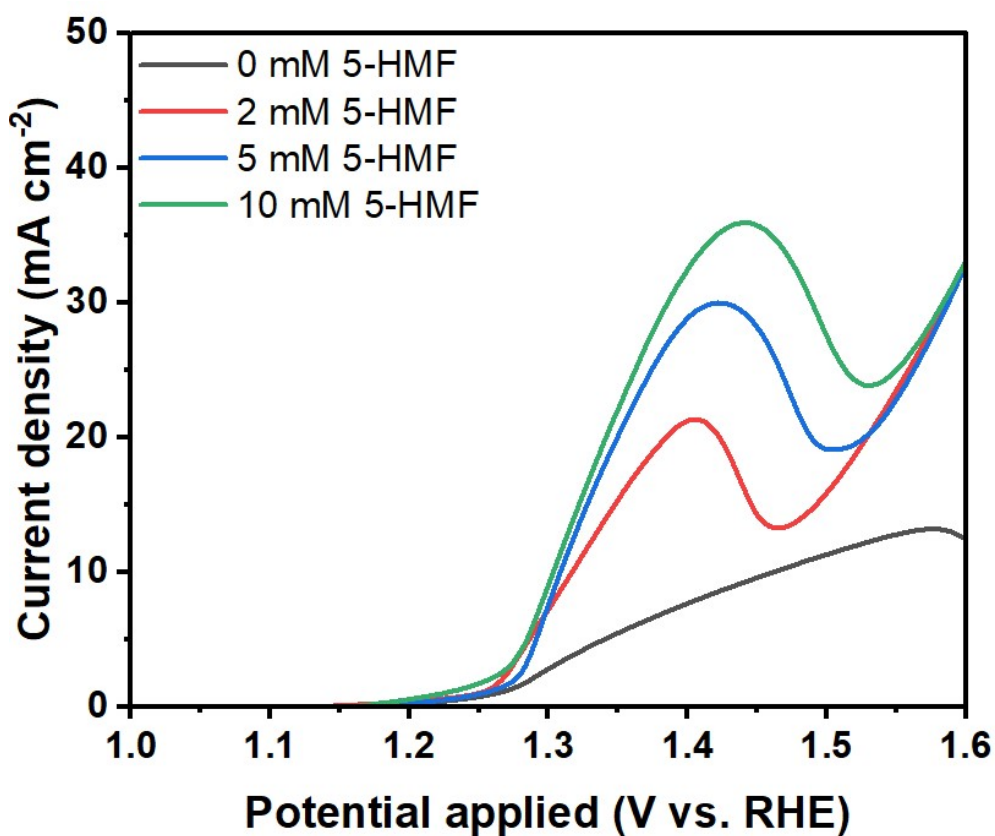


**Fig. S8** LSV curves of 5-HMF electrooxidation over NiCNTs/NF (NiHieZSM-5-CNTs) when varying concentrations of HMF (0-10 mM) in 1 M KOH at a scan rate of 20  $\text{mV s}^{-1}$ .

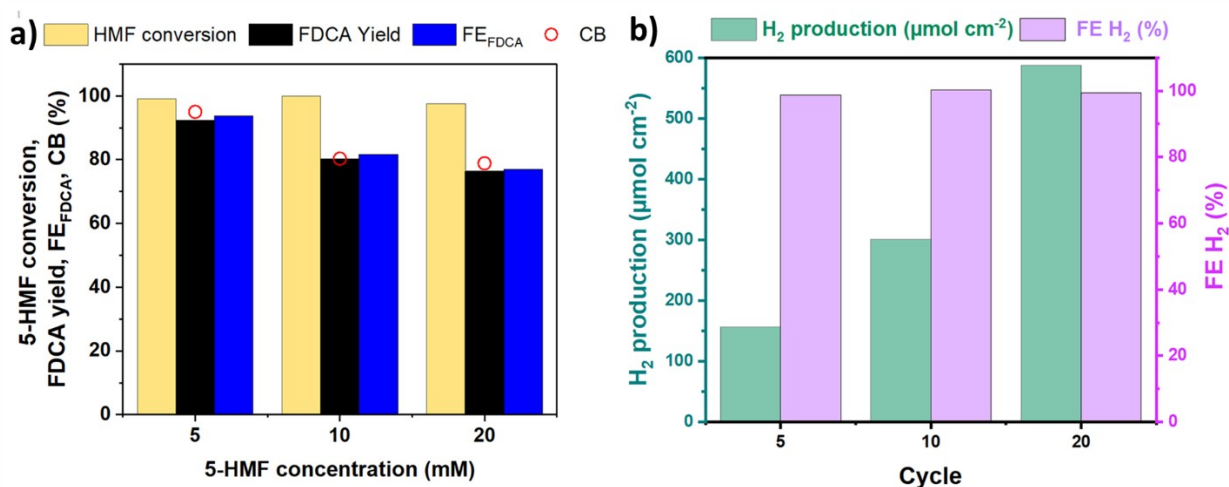


**Fig S9.** Electrocatalytic performances reported for varied concentration of 5-HMF over NiCNTs/NF for (a) 5-HMF oxidation ( $FE_{FDCA}$ ) at the anode from 5 to 20 mM of 5-HMF (b) simultaneous HER at the cathode ( $FE_{H_2}$ ). The figure shows HMF conversion (yellow), FDCA yield (black),  $FE_{FDCA}$  (dark blue),  $CB_{FDCA}$  (red dot), hydrogen production (green), and  $FE_{H_2}$  (purple).

As shown in Fig. S9, experiments were conducted using 5 mM, 10 mM, and 20 mM concentrations of 5-HMF. The NiCNTs catalyst consistently achieved nearly 100% conversion of 5-HMF at all concentrations. However, the yield of FDCA decreased as the concentration increased, with yields of 92.4% at 5 mM, 80.3% at 10 mM, and 76.4% at 20 mM. The selectivity for FDCA was higher and more stable at the 5 mM concentration compared to the higher concentrations.

At the higher concentrations (10 mM and 20 mM), a noticeable decline in catalytic performance was observed, along with a significant drop in the carbon balance of 80.3% and 78.9%, respectively, compared to the 5 mM concentration (92.4%). This indicates the possible formation of undetectable side products<sup>5</sup>. Additionally, the reaction solution at higher concentrations changed to yellow, which was not present at 5 mM 5-HMF.

The amount of hydrogen produced at these potentials closely matched the theoretical values. For example, with a charge of 30.5C, 57.9C, and 114.1C passed at 1.45V, hydrogen amounts of 156.4, 301, and 587  $\mu\text{mol cm}^{-2}$  were produced, respectively, when all electrons were efficiently transferred to the cathode. The Faradaic efficiency for hydrogen generation was 98.7%, 100.1%, and 99.3%, respectively, for 5 mM, 10 mM, and 20 mM 5-HMF, indicating unchanged catalytic performance for  $H_2$  production when increasing the concentration of 5-HMF.



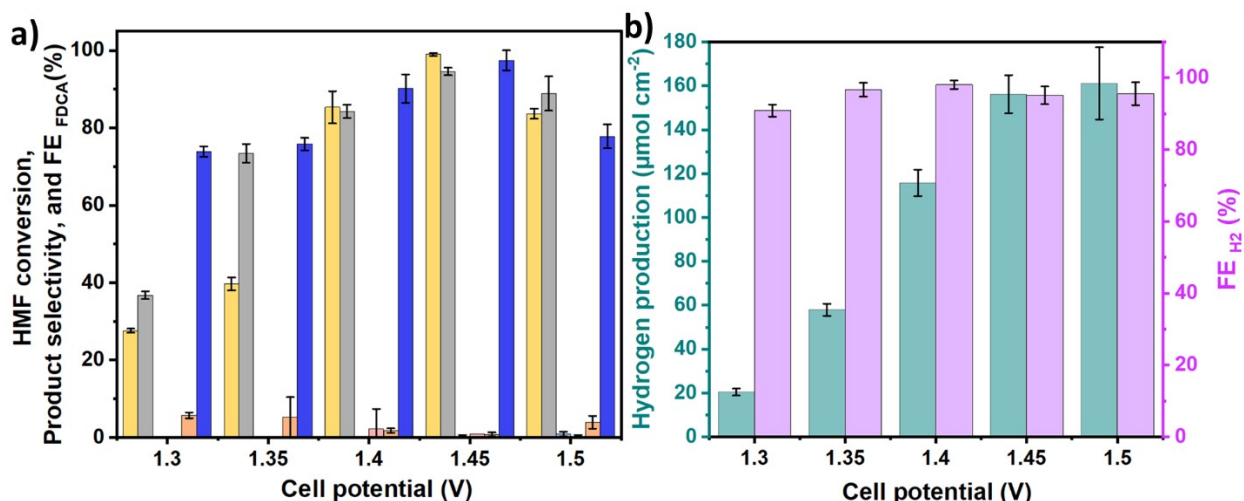


**Fig. S10** Electrochemical performances reported for the cell potential optimization over NiCNTs/NF for (a) 5-HMF oxidation (FE<sub>FDCA</sub>) at the anode with (b) simultaneous HER at the cathode (FE<sub>H₂</sub>). The figure shows HMF conversion (yellow), product selectivity for FDCA (grey), FFCA (light blue), DFF (pink), HMFA (orange), FE<sub>FDCA</sub> (dark blue), hydrogen production (green), and FE<sub>H₂</sub> (purple).

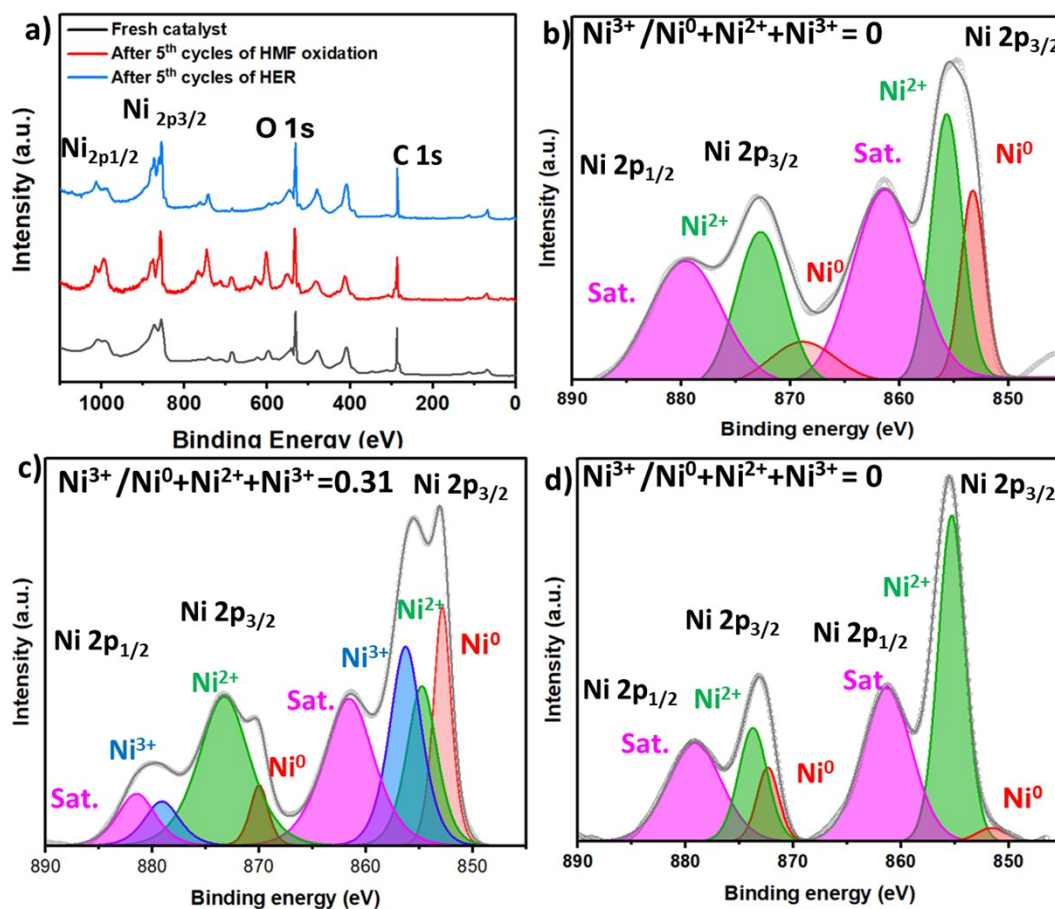


**Fig. S11** XPS spectra of NiCNTs/NF (5 wt.% NiHieZSM-5) showing (a) XPS survey scan and (b) high-resolution spectra of (b) the fresh catalyst, (c) after catalyzing five cycles of HMF oxidation, and (d) after catalyzing five cycles of the hydrogen evolution reaction.

**Table S4** XPS survey spectra quantification

Sample	% C1s	% O1s	%Ni 2p <sub>3/2</sub>	%Ni 2p <sub>1/2</sub>
NiCNTs/NF fresh	42.5	28.4	15.8	13.3
NiCNTs/NF after 5 <sup>th</sup> cycle of HMF oxidation	46.2	27.4	13.7	12.7
NiCNTs/NF after 5 <sup>th</sup> cycle of HER	43.8	29.9	15.4	10.8

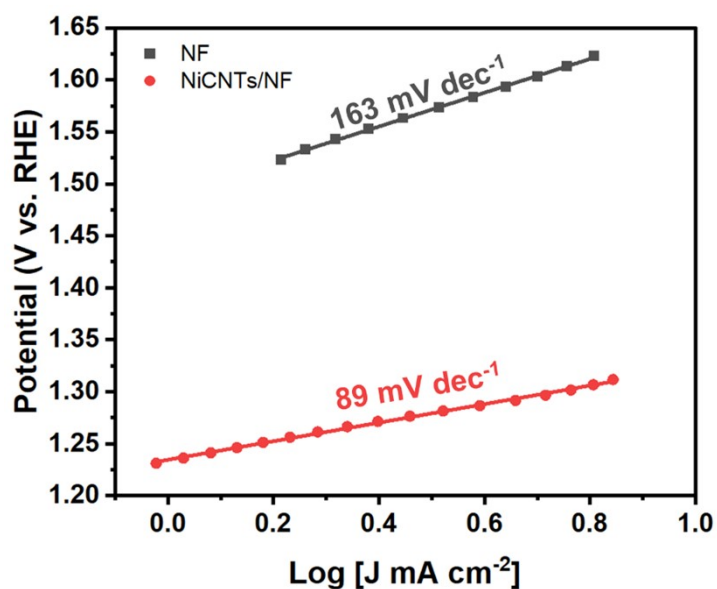
**Table S6** ICP Analysis NiCNTs/NF after five catalytic cycles

Sample	% leaching of Ni with respect to the fresh NiCNTs/NF
NiCNTs/NF after 5 <sup>th</sup> cycle of HMF oxidation	0.47
NiCNTs/NF after 5 <sup>th</sup> cycle of HER	1.56

**Table S6** ICP Analysis of % Weight of Nickel

Sample	%Weight of Ni
5wt.% NiHieZSM-5-CNTs	6.3
NiCNTs	3.4

The hydrofluoric acid (HF) treatment resulted in a significant reduction in nickel (Ni) content, as evidenced by the 46% decrease in Ni weight percentage from 6.3% to 3.4%. This suggests that Ni not strongly integrated with the CNTs structures, particularly the Ni associated with the zeolite that did not undergo CNTs growth, was more susceptible to leaching. However, the majority of Ni that was well incorporated into the CNTs remained stable despite the HF treatment, indicating the protective role of CNTs structures in preventing extensive Ni dissolution. These results highlight that the HF treatment selectively affects the Ni that is loosely bound to the zeolite, while Ni decorated on CNTs remains relatively unaffected. This conclusion supports the robustness of NiCNTs under HF extraction conditions, as detailed in Table S6.

**Fig. S12** Tafel slope of different catalysts in 1.0 M KOH.



The Tafel slopes for the NiCNTs/NF and NF electrodes were 89.2 mV dec<sup>-1</sup> and 162.5 mV dec<sup>-1</sup>, respectively. The lower Tafel slope for the NiCNTs/NF electrode indicates more favorable kinetics for the electrochemical oxidation process, likely due to high electrical conductivity and large surface area of CNTs, facilitating faster electron transfer rates at the electrode/electrolyte interface. The efficient electron transfer within the carbon network reduces charge transfer resistance, thereby enhancing the reaction kinetics and leading to higher current densities at given overpotentials.<sup>6</sup>

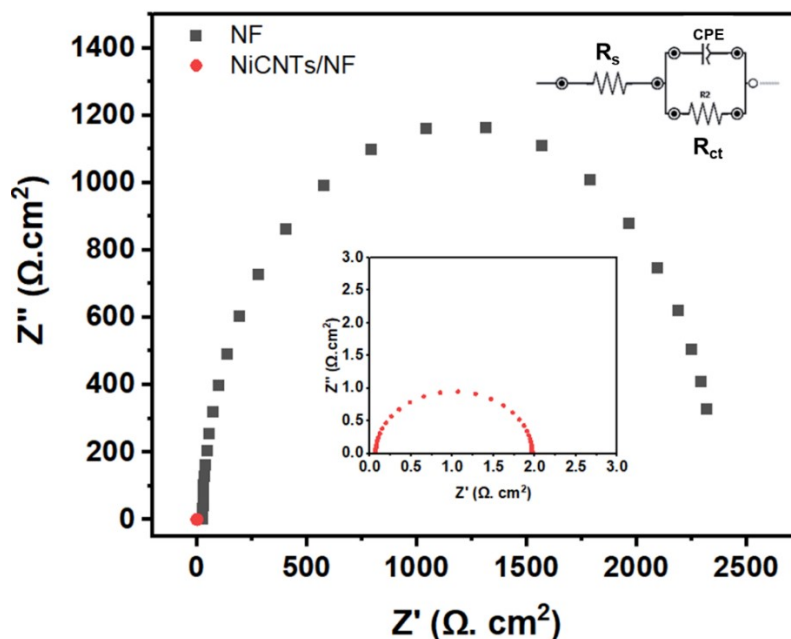


**Fig. S13** Nyquist plots compare the electrochemical impedance of two different electrodes: NiCNTs/NF and NF), in a 1 M KOH electrolyte. The inset zooms in on the Nyquist plot of the NiCNTs/NF electrode. EIS parameters: bias potential = 0 V, amplitude = 5 mV, and frequency = 0.01 Hz to 100 kHz.

The Nyquist plots clearly demonstrate the differences in electrochemical behavior between the NiCNTs/NF and the bare NF electrodes. The semicircle observed in the Nyquist plot represents the charge transfer resistance at the electrode-electrolyte interface. Notably, the NiCNTs/NF electrode exhibited a significantly lower  $R_{ct}$  (1.5  $\Omega$ ) compared to the bare NF electrode (2248  $\Omega$ ), indicating a marked improvement in electron transfer kinetics. This enhancement is likely due to the increased electronic conductivity of the NiCNTs composite material. The reduced charge transfer resistance observed for NiCNTs/NF directly correlates with the improved electrochemical performance, suggesting more efficient electron transport during the redox process. The enhanced electron transfer between carbon nanotubes (CNTs) is facilitated by their high aspect ratio and strong van der Waals interactions, which maintain close contact and reduce potential barriers for electron movement. These properties of CNTs significantly reduce the charge transfer resistance in electrochemical systems, making them highly effective in enhancing catalytic activity.<sup>7</sup> Furthermore, the Randles circuit model used to analyze the EIS data provides a clear representation of the system's electrochemical behavior, reinforcing the mechanistic understanding of how the modification with NiCNTs improves the catalytic properties of the nickel foam. This improvement in the charge transfer process underpins the superior catalytic activity observed in our other electrochemical measurements.

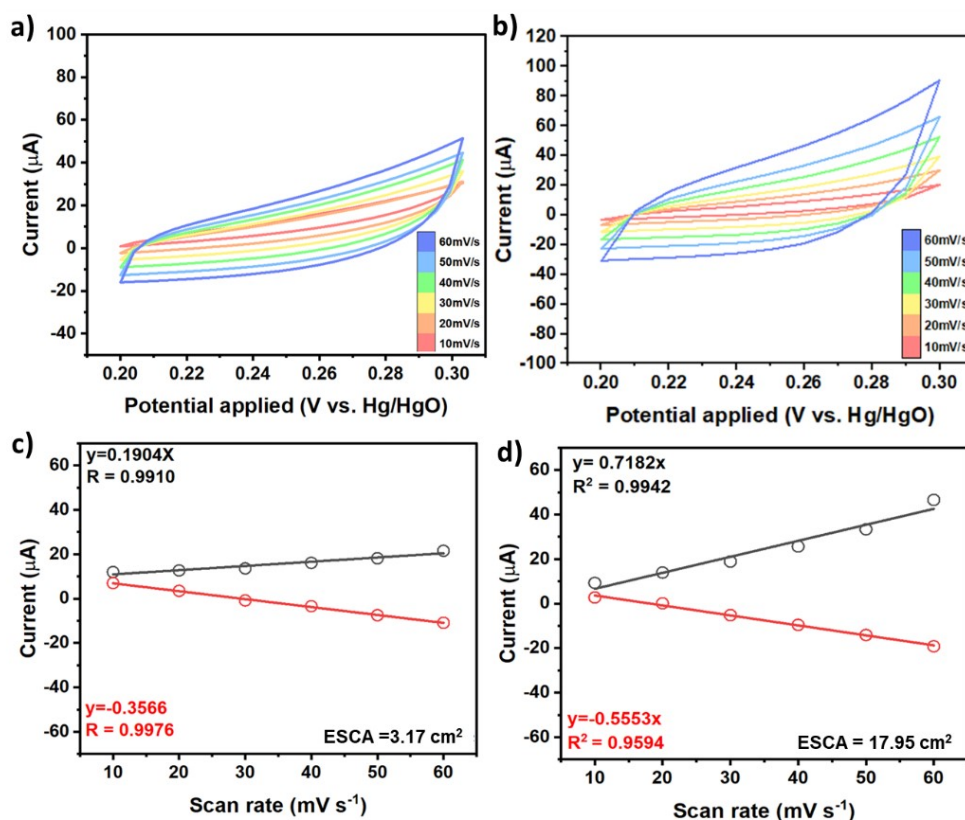


**Fig. S14** Cyclic voltammograms (CV) in the non-Faradaic region of (a, c) nickel foam, (b) NiCNTs/NF(NiHieZSM-5-CNTs) and (c, d) corresponding relationship between current and scan rate ranging from 10 to 60  $\text{mV s}^{-1}$

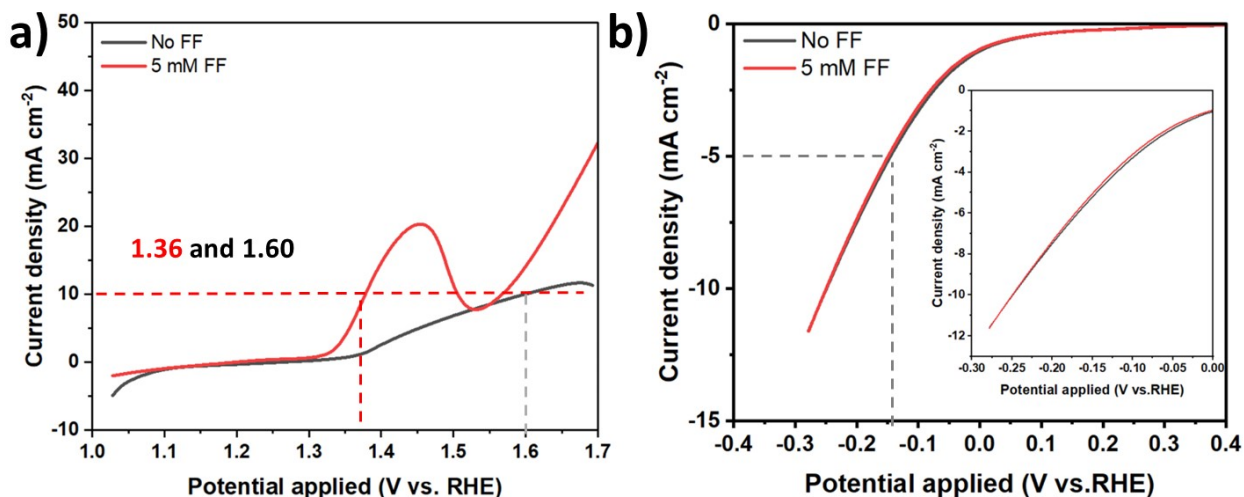


**Fig. S15** (a) LSV curves of (a) FF oxidation, (b) HER over the synthesized NiCNTs/NF catalyst in 1.0 mM KOH with and without 5mM FF at a scan rate of 20  $\text{mV s}^{-1}$ .

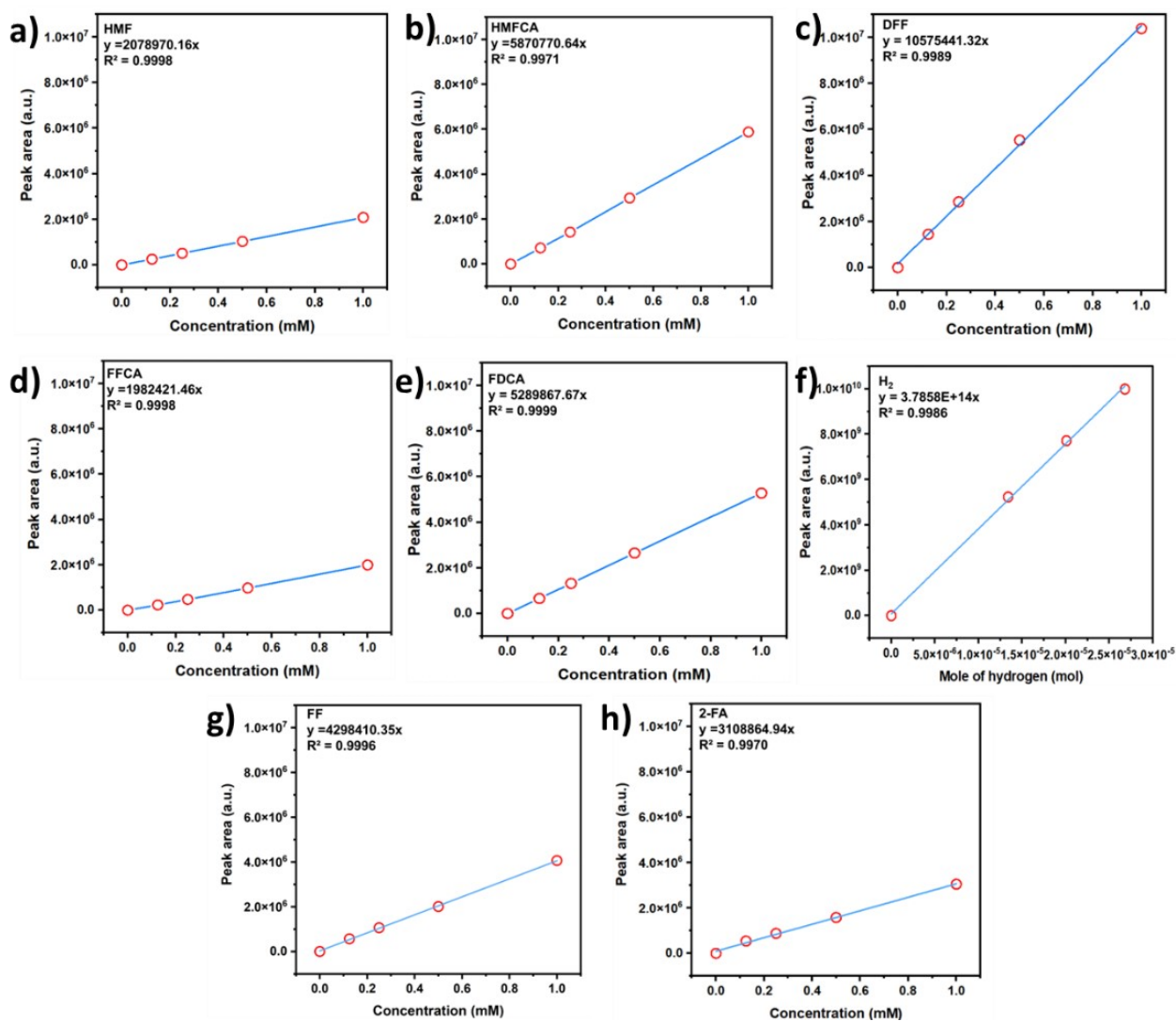


**Fig. S16** Calibration curves of the integrated peak area obtained from HPLC and GC measurements for (a) 5-HMF, (b) HMFCA, (c) DFF, (d) FFCA, (e) FDCA, (f) H<sub>2</sub>, (g) FF, and (h) 2-FA.

**Table S7** Comparison of Electrocatalytic Studies on Furan Derivatives Oxidation and H<sub>2</sub> Production

	Electrocatalyst	Reactant	Product	Conversion (%)	Yield (%)	FE (%)	Conditions	Ref.
1	Ni-decorated CNTs	HMF, furfural (FF)	FDCA, 2-FA, H <sub>2</sub>	HMF: 98.9 ± 1.3%, FF: 100%	FDCA: 94.6 ± 1.0%	FDCA: 97.4 ± 2.5%, H <sub>2</sub> : 93.7 ± 2.2%	Optimal potential of 1.45 V in 1 M KOH	<a href="#">In this work</a>
2	MnO <sub>x</sub> anode and a Pt anode	20 mM HMF	FDCA, H <sub>2</sub>	>99.9%	53.8%	FE <sub>FDCA</sub> 33.8% FDCA	At 60 °C and 2.0 V vs. RHE in H <sub>2</sub> SO <sub>4</sub>	<a href="#">8</a>
3	Ni(OH) <sub>2</sub> /NiOOH catalyst	HMF	FDCA,	90.4%	FDCA 83.9 %	n.a	0.1 M KOH	<a href="#">9</a>
4	Pt anode and Ni cathode	Furoic Acid (2-FA)	GBL, H <sub>2</sub>	69.1%	84.2% for FA to 2(5H)-furanone, 98.5% for GBL	38.3%	Undivided cell at 80°C, +2.0 V vs. Ag/AgCl in 0.5 M H <sub>3</sub> PO <sub>4</sub> , KH <sub>2</sub> PO <sub>4</sub> , and K <sub>2</sub> HPO <sub>4</sub>	<a href="#">10</a>
5	Ni <sub>2</sub> P NPA/NF	10 mM HMF	FDCA, H <sub>2</sub>	>99%	>99% for FDCA	~98 % and 100% for FE <sub>FDCA</sub> and H <sub>2</sub>	1.0 M KOH	<a href="#">11</a>

## References

1. P. Pornsetmetakul, S. Klinyod, C. Rodaum, S. Salakhum, P. Iadrat, E. J. M. Hensen and C. Wattanakit, *ChemCatChem*, 2023, **15**, e202201387.
2. S. Shetsiri, A. Thivasasith, K. Saenluang, W. Wannapakdee, S. Salakhum, P. Wetchasat, S. Nokbin, J. Limtrakul and C. Wattanakit, *Sustain. Energy Fuels.*, 2019, **3**, 115-126
3. S. Tantisriyanurak, S. Klinyod, W. Leangsiri, W. Nunthakitgoson, A. Soyphet, M. Ketkaew, A. Thivasasith, P. Iadrat, C. Rodaum, T. Atitthep, M. T. Nguyen, T. Yonezawa and C. Wattanakit, *ACS Appl. Nano Mater.*, **6**, 8784-8794.
4. X. Lu and C. Zhao, *Nat. Commun.*, 2015, **6**, 6616.
5. D.-H. Nam, B. J. Taitt and K.-S. Choi, *ACS Catal.*, 2018, **8**, 1197-1206.
6. Y. Zheng, Y. Jiao, M. Jaroniec and S. Z. Qiao, *Angew. Chem. Int. Ed.*, 2015, **54**, 52-65.

7. H. Dai, *Acc. Chem. Res.*, 2002, **35**, 1035-1044.
8. Y. Yang, T. Mu, *Green Chem.*, 2021, **23**, 4228-4254.
9. T. Harhues, M. Padligur; F. Bertram, D. M. Roth; J. Linkhorst, A. Jupke, M. Wessling, R. Keller, *ACS Sustain. Chem. Eng.*, 2023, **11**, 8413-8419.
10. S. Liu, Y. Jin, S. Huang, Q. Zhu, S. Shao and J. C.-H. Lam, *Nat. Commun.*, 2024, **15**, 1141.
11. S. R. Kubota and K.-S. Choi, *ChemSusChem*, 2018, **11**, 2138-2145.